Probing Structure and Ionic Transport in Molten Lithium Carbonate

Debsundar Dey[1], Abhirup Patra[2], Anand Narayanan Krishnamoorthy[3], and Gopalakrishnan Sai Gautam[1,*]

[1]Department of Materials Engineering, Indian Institute of Science, Bengaluru, 560012, India

[2]Shell International Exploration & Production Inc., 200 N Dairy Ashford Rd, Houston, TX 77079, United States

[3]Shell India Markets Pvt. Ltd. (Shell Projects & Technology), Mahadeva Kodigehalli, Bengaluru 562149, Karnataka, India

[*]Email: abhirup.patra@shell.com; saigautamg@iisc.ac.in

Abstract

Lithium carbonate (Li_2CO_3) is a cornerstone material for clean energy technologies, including high-temperature molten carbonate fuel cells, electrochemical carbon capture, and lithium-based batteries. However, capturing the complex, many-body interactions governing the structure and transport in Li_2CO_3, especially in its molten state, has remained a challenge, constrained by the computational cost of *ab initio* methods and the accuracy limitations of classical force fields. To address this gap, we deploy equivariant graph-based machine learned interatomic potentials, specifically, the multi atomic cluster expansion (MACE) and neural equivariant interatomic potential (NequIP) architectures that are trained on melt-quench *ab initio* molecular dynamics data. Our benchmarking demonstrates that MACE, utilizing higher body-order message passing, provides superior transferability and precision in predicting energies and forces compared to NequIP. Subsequently, we use the optimized MACE model to perform large-scale molecular dynamics simulations to probe the structural and transport properties of molten Li_2CO_3. Besides describing the structural features, such as the dominant presence of C-O pair correlations under molten conditions, our MACE model also reproduces experimentally-measured static structure factors and shear viscosity values. Further, our simulations indicate that Li^+ transport in Li_2CO_3 is fundamentally dominated by concerted motion, as evidenced by Haven's ratios being significantly below unity ($\approx 0.20 - 0.40$). Notably, we identify a temperature-driven transition from anisotropic (and highly concerted) Li^+ transport, supported by persistent oxygen-centered Voronoi cages at 1000 K, to isotropic (and less concerted) diffusion at 1400 K. Thus, we provide fundamental insights into the structural and transport properties of molten Li_2CO_3 and also demonstrate a robust and scalable framework for the accelerated design of molten salt electrolytes and ionic liquids for clean energy applications.

Introduction

Molten alkali carbonates represent a critically important class of ionic liquids with wide-ranging technological applications in clean energy systems [1]. For example, the high-temperature ionic melts serve as electrolytes in molten carbonate fuel cells (MCFCs), which operate at temperatures of 600- 700 °C and achieve electrical efficiencies approaching 60%, with combined heat and power efficiencies reaching 85% [2, 3]. Among the alkali carbonates, lithium carbonate (Li_2CO_3) plays a particularly prominent role due to its superior ionic conductivity compared to sodium and potassium carbonates [4, 5]. Standard MCFC electrolytes typically contain 62−68 mol% Li_2CO_3 mixed with K_2CO_3 or Na_2CO_3, with the lithium component providing enhanced ionic transport while the secondary carbonate reduces corrosion and improves gas solubility [6,7]. Beyond fuel cells, molten Li_2CO_3 has emerged as a promising medium for electrochemical CO_2 capture and subsequent conversion to valuable carbon nanomaterials, including carbon nanotubes and graphene nanocarbons, offering a pathway for large-scale decarbonization [8, 9].

Despite their technological importance, achieving a fundamental, atomistic understanding of the structure and dynamics of molten carbonates remains challenging. The extreme chemical reactivity of these melts at elevated temperatures, combined with their corrosive nature, presents significant obstacles for experimental characterization of atomic structures and transport properties [10, 11]. Experimental techniques such as X-ray and neutron scattering can provide structural information through the static structure factor ($S(q)$) and radial distribution functions (RDFs, denoted by $G(r)$ or $g(r)$), while electrochemical methods and pulsed-field gradient nuclear magnetic resonance can probe transport coefficients [12–14]. However, these measurements are technically demanding and provide limited insight into the microscopic mechanisms governing ionic transport, particularly the nature of correlated ionic motion that deviates from the ideal Nernst-Einstein behavior. Resolving whether ionic transport in these melts follows a traditional, independent random-walk model or a more complex, many-body correlated mechanism, and the local structural motifs that influence macroscopic conductivity are essential for the optimal design of high-performance electrolytes that enhance ionic conductivity and reduce interfacial resistance.

Beyond their importance in molten carbonate systems, lithium carbonates are also technologically relevant in Li-ion batteries [15–18]. Li_2CO_3 is one of the dominant inorganic constituents of the solid electrolyte interphase (SEI), where it forms crystalline and amorphous domains that govern Li^+ transport across the electrode-electrolyte interface [19–22]. The SEI stabilizes the anode by preventing continuous electrolyte decomposition, but it also introduces additional interfacial resistance, making Li^+ mobility through Li_2CO_3-rich domains a critical determinant of fast-charging performance and long-term cycling stability [23–25]. The contrasting Li^+ conductivities of crystalline and amorphous Li_2CO_3, as well as the mixed-phase and polydomain character of realistic SEIs, highlight the broader importance of understanding Li ionic transport in Li_2CO_3 across both solid and molten regimes.

Atomistic simulation provides a powerful complementary approach for elucidating the structure-property relationships in molten salts. Classical molecular dynamics (MD) simulations based on empirical force fields, such as rigid-ion or polarizable shell models, have been widely employed to study molten carbonates [26–28]. While computationally efficient, these classical potentials often struggle to accurately capture the complex many-body interactions and polarization effects that are critical in ionic systems. *Ab initio* molecular dynamics (AIMD) based on density functional theory (DFT) offers quantum mechanical accuracy but is computationally prohibitive for accessing the long time scales (hundreds of picoseconds to nanoseconds) and large system sizes (thousands of atoms) required for converged transport properties and proper sampling of the liquid structure [29, 30]. This fundamental trade-off between accuracy and computational efficiency has

motivated the development of machine learned interatomic potentials (MLIPs) that can achieve near-DFT accuracy at a fraction of the computational cost of AIMD simulations.

Various MLIP architectures have been successfully applied to molten salts and related systems, including neural network potentials, Gaussian approximation potentials (GAP), moment tensor potentials (MTP), and deep potential molecular dynamics (DeepMD) [31–36]. Similar successes have been reported for diverse molten salt chemistries relevant to energy conversion, nuclear applications, and high-temperature electrochemical technologies [34, 37, 38]. Recently, MLIPs have also been used for characterizing ionic transport across amorphous materials and their interfaces in battery systems [39, 40]. So far, equivariant MLIPs have not been used to probe the transport and local structure motifs in molten Li_2CO_3.

Recent advances in equivariant neural network architectures have further improved the accuracy and data efficiency of MLIPs. For example, E(3)-equivariant graph-based neural networks, which explicitly include the symmetries of three-dimensional space (i.e., translations, rotations, and reflections), along with message passing, provide a better representation of atomic environments compared to invariant neural networks [41, 42]. Specifically, the neural equivariant interatomic potential (NequIP) architecture employs E(3)-equivariant convolutions to describe geometric tensors, achieving high accuracy with remarkable data efficiency that outperforms invariant approaches with up to three orders of magnitude fewer training data [43]. Building upon NequIP, the multi atomic cluster expansion (MACE) architecture introduces higher body-order message passing, enabling the capture of many-body interactions (typically up to four-body terms). By explicitly accounting for such many-body interactions, MACE is uniquely positioned to resolve the subtle, concerted ion-ion interactions that govern transport in molten carbonates—features that are often missed by traditional invariant potentials [44,45]. Given the utility in incorporating equivariance, message passing and many-body interactions (in MACE), both NequIP and MACE have been successfully applied to challenging systems, such as, ionic liquids, water, amorphous solids, and complex molecular systems [40, 46–51].

In this work, we construct and assess equivariant MLIPs and subsequently probe the structural and transport properties in molten Li_2CO_3. We construct the MLIPs based on AIMD training data, with training configurations sampling melt–quench trajectories at 1500 K and 1250 K, resulting in 3600 and 1988 structures, respectively. To assess model fidelity against AIMD and available experimental data, we use RDFs and $S(q)$ as metrics. We train both the MACE and NequIP architectures on our dataset, from scratch, and identify MACE to be the best model based on the train and test mean absolute errors (MAEs) across energies and forces. Additionally, we evaluate the medium-sized MACE-MP-0 model [52], a foundational pre-trained MLIP without fine-tuning, to benchmark structural accuracy. Using the best-performing potential, i.e., MACE architecture trained from scratch, simply referred to as MACE in the remainder on the text, we perform long time-scale MD simulations to compute macroscopic transport properties, including the shear viscosity and Li^+ self-diffusion coefficients.

Importantly, we find the activation energy of Li^+ diffusion (E_a), calculated based on an Arrhenius fit of Li^+ diffusivities over temperatures to be 1.287 eV, which is consistent with prior molten-salt literature [25]. Our analysis of ionic trajectories reveals distinct temperature-dependent diffusion mechanisms. For example, at 1400 K, Li^+ exhibit continuous migration through the molten carbonate network, while at 1000 K transient trapping events emerge, wherein Li^+ oscillate between nearby carbonate coordination cages before escaping. Large-scale simulations enabled by the optimized MACE potential further show that Li-ion transport in molten Li_2CO_3 is fundamentally collective, with Haven's ratio (H_R) values significantly below unity ($H_R \sim$ 0.20–0.40). Finally, we identify a temperature-driven transition from anisotropic transport at 1000 K to isotropic diffusion at 1400 K, demonstrating the ability of equivariant MLIPs to resolve complex transport

behavior across different molten carbonate regimes. We hope that our work is a useful contribution in the optimal design of molten salt electrolytes for MCFCs and related applications.

Dataset Generation and Optimized MLIPs

Figure 1 summarizes the overall workflow of this study, including AIMD-based data generation, MLIP training and validation, and subsequent molten-phase simulations performed using the optimized model. To develop and evaluate MLIPs for molten-Li_2CO_3, we generated a dataset using AIMD melt-quench simulations [53, 54] on a $2 \times 2 \times 2$ supercell (192 atoms) of the crystalline Li_2CO_3 structure that was obtained from the inorganic crystal structure database (ICSD [55]). We applied stepwise heating initially from 0 K to 500 K, subsequently from 500 K to 1000 K, and finally from 1000 K to 1500 K, with each heating step conducted over 5 ps followed by 2 ps of equilibration. The choice of 1500 K as the highest temperature in our heating simulations is motivated by the fact that Li_2CO_3 melts at 996 K [56]. Subsequently, we quenched the equilibrated structure at 1500 K to 1000 K, in steps of 250 K at a quench rate of 83.33 K/ps. For training, we sampled configurations from AIMD trajectories at 1500 K (accounting for 3600 structures sampled over 7.2 ps) and at 1250 K (1988 structures sampled over 3.98 ps), with the training data collected after the initial 2 ps of equilibration at each temperature.

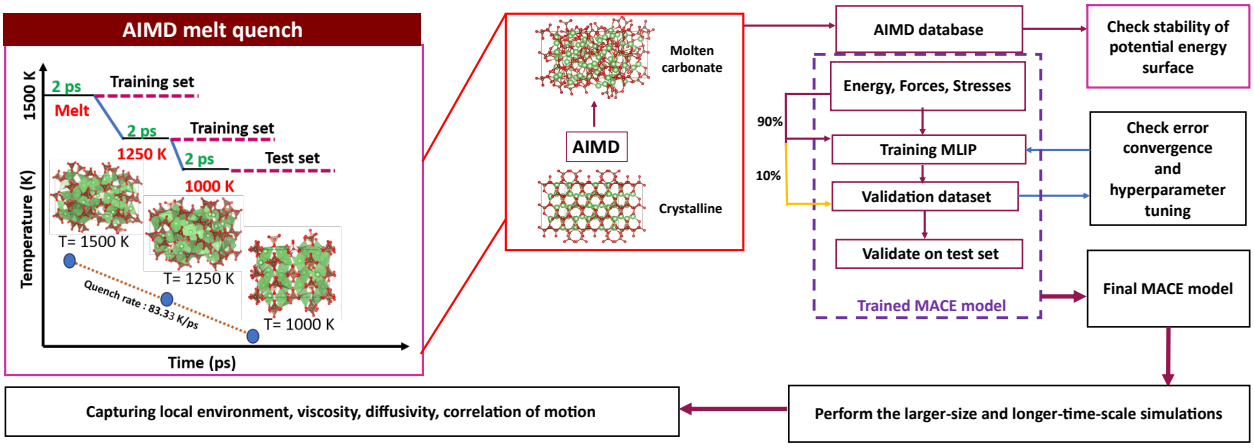

Figure 1: Workflow for dataset generation and MLIP training (for MACE) employed in this work. We employ AIMD melt-quench simulations both for training and hyperparameter optimization. The accuracy and transferability of the trained MLIP are evaluated using independent test configurations. After validation, the optimized MACE model is deployed for long time-scale and large system-size MD simulations to characterize transport properties of molten-Li_2CO_3.

We trained both NequIP and MACE models using the dataset generated from the AIMD melt-quench simulations. We performed training and hyperparameter optimization on the AIMD-derived training dataset, by creating a 90:10 train:validation split of the dataset. The list of optimal hyperparameters that were chosen to minimize errors on the validation set for both models are listed in **Tables S1** and **S2** of the supporting information (SI). To ensure a fair comparison, we set the equivariance level of both models to one (i.e., $L_{\max} = 1$). We evaluated the performance of both models using MAEs across both total energies and atomic forces. We used two separate test datasets to evaluate the transferability of the trained MLIPs: (i) configurations from AIMD, post quench, at 1000 K, and (ii) mechanically strained structures of crystalline-Li_2CO_3, including homogeneous volumetric strain ($\pm$2%, $\pm$5%, $\pm$10%), uniaxial strain ($\pm$2%, $\pm$5%, $\pm$10%), and shear strain (2%, 5%, 10%). To verify that the sampled configurations correspond to the molten phase

of Li_2CO_3, we computed the RDFs for all relevant atomic pairs ($G(r)$), namely O-O, Li-Li, C-O, Li-O, C-C, and Li-C.

DFT and MD calculations

We utilized the Vienna *ab initio* simulation package [57,58] with projector augmented wave potentials [59] to perform all spin-polarized DFT and AIMD calculations. We used the Perdew-Burke-Ernzerhof functionalization of the generalized gradient approximation [60] to account for the electronic exchange and correlation. We applied a kinetic energy cutoff of 520 eV, and sampled the irreducible Brillouin zone using Γ-centered Monkhorst-Pack k-point meshes with a density of at least 32/Å [61]. We relaxed the as-obtained crystalline Li_2CO_3 structure (from the ICSD) by optimizing the cell volume, cell shape, and atomic positions without imposing symmetry constraints before performing AIMD simulations and generating the strained structure dataset. We set the convergence criteria for total energy and atomic forces to 10^{-5} eV and |0.03| eV/Å, respectively. For generating the strained structure dataset, we deformed the DFT-relaxed Li_2CO_3 lattice with the corresponding amount of strain and evaluated the total energy using a single self-consistent field calculation (with energy convergence set to 10^{-5} eV) without any further relaxation of the structure.

We performed AIMD simulations on a $2 \times 2 \times 2$ supercell of Li_2CO_3, corresponding to 192 atoms, using a 2 fs time step to ensure accuracy and efficiency. We did classical MD simulations with our trained MACE model using the large scale atomic/molecular massively parallel simulator (LAMMPS) [62]. We employed a 2 fs time step for the classical MD simulations and used a $4 \times 4 \times 4$ supercell containing 1536 atoms. All AIMD and MD runs employed the NVT ensemble with a Nosé-Hoover thermostat [63], the '`SMASS`' tag set to 0, and the velocity-Verlet integration scheme [64]. For MD simulations with the MACE model trained from scratch, we equilibrated the structures in the NVT ensemble for 10 ps, followed by 700 ps of production runs to estimate diffusivities at 1500 K, 1400 K, 1300 K, 1250 K and 1000 K. The variations in potential energy (in eV), as estimated by MACE during the 10 ps equilibration period, at 1000 K, 1250 K, 1300 K, and 1400 K are shown in **Figure S3**.

Estimation of diffusivity, ionic correlation, and viscosity

In molten Li_2CO_3, ionic conductivity (σ) and diffusivity ($D(c)$) of any species, such as Li^+, are connected through the Nernst-Einstein (NE) relation as,

$$\sigma = \frac{q^2\, cD(c)}{k_B T} \tag{1}$$

where q, c, k_B, and T represent the ion's charge (+1 in case of Li^+), the ion's concentration, the Boltzmann constant, and temperature, respectively. While the NE relation provides an estimate of σ assuming uncorrelated ionic motion, molten salts generally exhibit strong many-body interactions, leading to significant correlations. Therefore, the calculated σ from NE can systematically deviate from the true σ, with the correlation effects requiring further quantitative analysis, such as using H_R [65]. $D(c)$ in the NE framework describes the ionic flux according to Fick's first law [66] and can be expressed as $D_c = \Theta D_J$, where Θ is the thermodynamic factor. The jump diffusivity (D_J [67, 68]) measures the mean squared displacement of the center-of-mass of the mobile ions (denoted as 'MSCD' in our work), thus capturing cross-correlations among

individual ionic hops over time. Mathematically, D_J is defined as,

$$D_J = \lim_{t\to\infty} \left[\frac{1}{2dt} \frac{1}{N} \left(\sum_{i=1}^{N} \mathbf{r}_i(t) \right)^2 \right] \tag{2}$$

where d, t, and N represent the dimensionality of the diffusion process, time, and number of mobile ions, respectively. $r_i(t)$ indicates the displacement of the i^{th} ion over t.

On the other hand, the tracer diffusivity (D^*) tracks the motion of individual ions thereby not accounting explicitly for any cross-correlations among their motion. Specifically, D^* quantifies the mean squared displacement (MSD) that is averaged over N and t and is mathematically defined as,

$$D^* = \lim_{t\to\infty} \left[\frac{1}{2dt} \frac{1}{N} \sum_{i=1}^{N} [\mathbf{r}_i(t)]^2 \right] \tag{3}$$

Note that D_J and D^* can be obtained from the slopes of the linear regimes of MSCD and MSD values, respectively, with respect to t [67]. Finally, H_R is defined as the ratio of D^* and D_J as,

$$H_R = \frac{D^*}{D_J} \tag{4}$$

Thus, H_R provides insight into how cross-correlations alter the overall ionic mobility. If a system exhibits completely uncorrelated ionic motion, $H_R = 1$. In systems with significant ion–ion interactions, H_R deviates from 1, indicating the presence of cross-correlation. Note that in molten Li_2CO_3, we do expect cross-correlation effects to be significant since Li^+ transport does not occur in isolation and is often influenced by the rearrangements in the carbonate network and the local charge neutrality.

Due to the limited total simulation time (t_{tot}) in both AIMD and classical MD, MSD data often exhibits noise, leading to fluctuations in the estimated slope versus t. To reduce this statistical variability, we employed the total mean-squared displacement (TMSD, Equation 5), which averages the MSD over multiple time intervals (Δt), following the approach of He et al. [67].

$$\text{TMSD}(\Delta t) = \sum_{i=1}^{N} \left[\frac{1}{N_{\Delta t}} \sum_{t=0}^{t_{\text{tot}}-\Delta t} |\mathbf{r}_i(t+\Delta t) - \mathbf{r}_i(t)|^2 \right] \tag{5}$$

Here, $N_{\Delta t}$ denotes the number of possible time intervals of duration Δt. D^* is subsequently determined from the slope of MSD versus Δt, subject to ranges of Δt values for which MSD behaves linearly.

$$D^* = \frac{\text{MSD}(\Delta t)}{2d\Delta t} \tag{6}$$

where $\text{MSD}(\Delta t) = \text{TMSD}(\Delta t)/N$. A similar approach can be used for estimating D_J as well [67]. In this work, we set $\Delta t = 50$ ps for all diffusivity calculations because it provides a sufficiently long window to access diffusive behavior while maintaining adequate averaging statistics within the total trajectory length ($t_{\text{tot}} =$ 700 ps). Also, the MSD exhibits linear scaling with Δt in this regime. We used the `DiffusionAnalyzer` class of `pymatgen` [69, 70] for post-processing our AIMD and classical MD calculations and determining D_J, D^* and H_R.

Finally, in an ideal transport regime, where ionic hops occur with uniform frequency and are unaffected by local compositional fluctuations or structural heterogeneity, the overall diffusion coefficient (D_J or D^*,

denoted as D below) takes the Arrhenius form,

$$D = D_0 \exp\left(-\frac{E_a}{k_B T}\right) \tag{7}$$

The pre-exponential factor D_0 encapsulates parameters such as the hop distance, the atomic vibrational frequency, the available diffusion-carrier concentration, the correlation factor (which describes deviations from random walk), and the geometric factor (connectivity of pathways). The activation energy (E_a) for migration, a material-specific property, governs D exponentially and can be extracted from the slope of $\ln D$ versus $1/T$. Although D may depend on correlation and geometric factor, E_a is typically the dominant rate-limiting parameter and therefore a key quantity for assessing ionic transport performance.

For the calculation of the shear viscosity (η), we equilibrated the Li_2CO_3 system in the NVT ensemble for 50 ps, and collected the stress components collected during a 30 ps production run. Note that the viscosity is related to the time integral of the autocorrelation function of the off-diagonal stress-tensor components, within the Green-Kubo formalism [71, 72], as,

$$\eta = \frac{V}{3k_B T} \int_0^\infty \left[\langle P_{xy}(0)P_{xy}(t)\rangle + \langle P_{xz}(0)P_{xz}(t)\rangle + \langle P_{yz}(0)P_{yz}(t)\rangle\right] dt. \tag{8}$$

Here, V is the simulation cell volume, k_B is the Boltzmann constant, T is the temperature. $P_{\alpha\beta}$ represent the off-diagonal components of the pressure or stress tensor, where $\alpha\beta = xy, xz$, or yz. The angular brackets denote averaging over time.

Model comparison

To identify the best performing model, among NequIP and MACE, we compared the performance of both models on the training, validation, and test datasets. The parity plots for the MACE (panel **a**) and NequIP (panel **b**) models on the test AIMD dataset at 1000 K are shown in **Figure S1**, while **Figure S2** (panel **a** for MACE and panel **b** for NequIP) displays the corresponding results for the strained structures (test) dataset. For NequIP, the training energy MAE is 1.3 meV/atom and the validation energy MAE is 0.3 meV/atom. The corresponding force MAEs are 22.4 meV/Å and 0.31 meV/Å for the training and validation sets, respectively. In contrast, the MACE model exhibits superior accuracy, achieving training and validation energy MAEs of 0.1 meV/atom and force MAEs of 2.4 meV/Å and 3.3 meV/Å, respectively.

Evaluation on the independent test dataset at 1000 K further highlights the higher accuracy and improved transferability of the MACE model, with energy and force MAEs of 0.2 meV/atom and 0.17 meV/Å, respectively, compared to 2.6 meV/atom and 18.1 meV/Å for the NequIP model. For mechanically strained test structures, the MACE model achieves MAEs of 6.8 meV/atom for energies and 13.16 meV/Å for forces, while NequIP yields higher errors, with energy and force MAEs of 21.08 meV/atom and 24.49 meV/Å, respectively. These results collectively demonstrate the enhanced accuracy and transferability of the MACE model compared to NequIP across the diverse evaluation scenarios considered. Accordingly, we employ the optimized MACE model for all subsequent large-scale and long time-scale MD simulations of molten Li_2CO_3.

Structural properties of molten Li_2CO_3

We used RDFs and $S(q)$ to characterize the structural properties of molten Li_2CO_3. Note that $S(q)$ plays a particularly important role, as it is directly accessible via experimental techniques such as X-ray and

neutron scattering. We examine the RDFs of all atomic pairs to resolve the short- and medium-range structural ordering within Li_2CO_3, as compiled in **Figure 2**. Note that we compiled RDFs of crystalline Li_2CO_3 (calculated with DFT), and molten Li_2CO_3 (above 1000 K, calculated with MACE) in **Figure 2**, with some complimentary RDF data generated by AIMD and MACE compiled in **Figures S4** and **S5**. The predicted RDFs by the NequIP and MACE-MP-0 models are provided in **Figures S7-S9**).

For crystalline Li_2CO_3 (**Figure 2a**), the DFT-calculated RDFs exhibit sharp and well-defined peaks, with distinct peaks appearing over long distances reflecting the presence of long-range periodicity in the lattice. After melt-quench to 1000 K and subsequent heating to 1500 K (with MACE, panels **b-d** of **Figure 2**), the RDF peaks progressively broaden and decrease in intensity with increasing temperature, indicating a gradual loss of long-range structural order and increased configurational disorder in the molten state. Indeed, the atomic configurations reveal a distinct progression from a periodic network of well-defined Li-O polyhedra in the crystalline phase (**Figure 2a**) to a fully disordered molten structure (**Figure 2d**), wherein the Li-centered coordination environments become increasingly distorted and non-uniform. We observe an exception to the trend of broadening RDF peaks for the C-O pair (cyan peak), where we find only a marginal reduction in the height of the first coordination peak, even at 1500 K. The lack of significant changes in the C-O peak highlights the strong covalent character of the C-O bond that preserves the planar carbonate geometry irrespective of temperature. Note that although the carbonate units remain locally intact across all temperatures, their orientations become progressively random with increasing temperature, resulting in the loss of medium- and long-range structural order.

At 1000 K (**Figure 2b** and **Figure S4a**), both MACE and AIMD calculations show pronounced ordering in Li_2CO_3, with a strong C-O peak at ∼1 Å, followed by additional peaks at ∼4 Å and ∼6 Å, although these higher-order peaks are significantly reduced in intensity compared to the crystalline state. Beyond ∼6 Å, no sharp peaks are observed, consistent with the loss of long-range periodicity. The Li-O pairs (green) also show significant peak broadening beyond ∼2 Å, while Li-C pairs (black) retain some medium-range ordering. Further, we compare the C-O RDF predicted by the DeepMD model of Dina *et al.* [73] at 1043.15 K with our MACE data at 1000 K, and find that we accurately reproduce the peak positions and broadening observed by the authors at ∼1.5 Å and ∼4 Å (see **Figure S6**). This agreement with literature data demonstrates that both models capture the local structural features of molten Li_2CO_3 reasonably well.

Upon increasing the temperature to 1300 K (**Figure 2c**, the Li-C, C-O, C-C (magenta), and Li-O peaks begin to develop shoulders and further broaden, particularly beyond ∼3 Å, ∼6 Å, ∼5 Å, and ∼4 Å, respectively. This progressive broadening confirms that the melt structure becomes increasingly disordered with temperature. At 1500 K (**Figure 2d** and **Figure S4c**), the Li-O peak at ∼2 Å, and the Li-C peak at ∼3 Å show reduced intensity accompanied by pronounced shoulder formation. We do not observe any discernible peaks beyond ∼6 Å, confirming the complete loss of long-range order and the molten state of Li_2CO_3.

Compared to AIMD data at 1500 K (**Figure S4c**), the MACE model exhibits similar RDFs (**Figure 2d**) except a marginally more pronounced shoulder broadening for the Li-C peak at ∼3 Å and a reduced broadening for the C-O and C-C peaks at ∼4 Å and ∼5 Å, respectively. On the other hand, the NequIP and MACE-MP-0 models correctly identify the peak positions in their predicted RDFs but fail to accurately reproduce the extent of peak broadening observed in AIMD across all temperatures (**Figures S7-S9**). Nevertheless, both NequIP and MACE-MP-0 successfully capture the melting of Li_2CO_3 above 1000 K, as evidenced by the complete loss of structural ordering beyond ∼6 Å.

We calculated the total RDF ($g(r)$) for molten Li_2CO_3 at different temperatures to further examine the

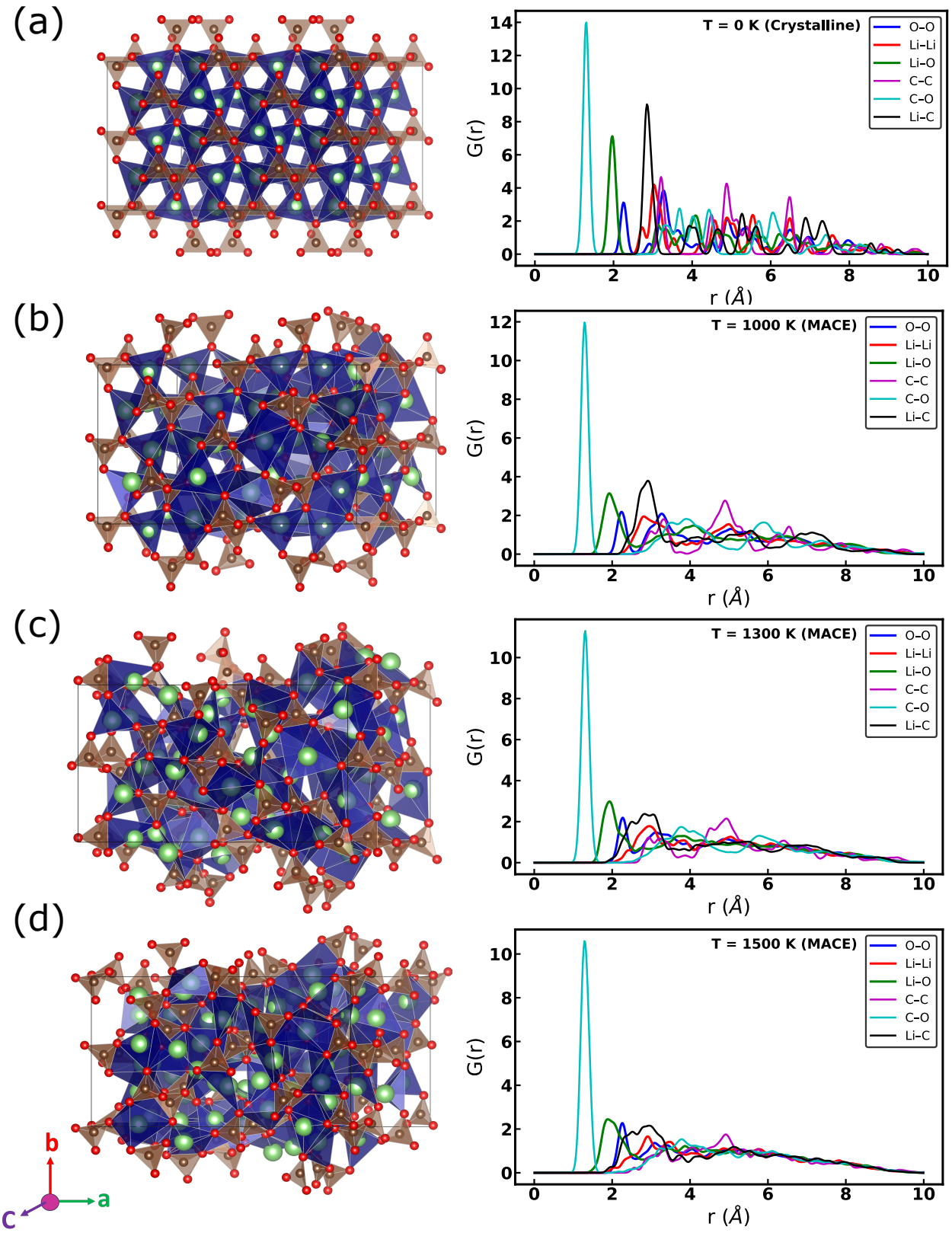

Figure 2: Representative atomic configurations (left panels) and corresponding RDFs ($G(r)$; right panels) of Li_2CO_3 at different temperatures. Panel a corresponds to crystalline Li_2CO_3 at 0 K relaxed using DFT, while the remaining panels show $G(r)$ for molten configurations generated using the optimized MACE potential at 1000 K, 1300 K, and 1500 K. Blue, red, green, magenta, cyan, and black curves correspond to $G(r)$ of O-O, Li-Li, Li-O, C-C, C-O, and Li-C pairs, respectively.

evolution of the Li_2CO_3 structure, as compiled in **Figure S10**. In the range of $2-4$ Å, the peaks exhibit a gradual shift and reduced peak intensity towards larger r values with increasing temperature, indicating a loss of short range order in the structure. At distances beyond ∼6 Å, the peaks become progressively broad and diminished at high temperatures (e.g., 1500 K), ultimately converging to $g(r) \approx 1$, which signifies the complete loss of long range order in the molten state.

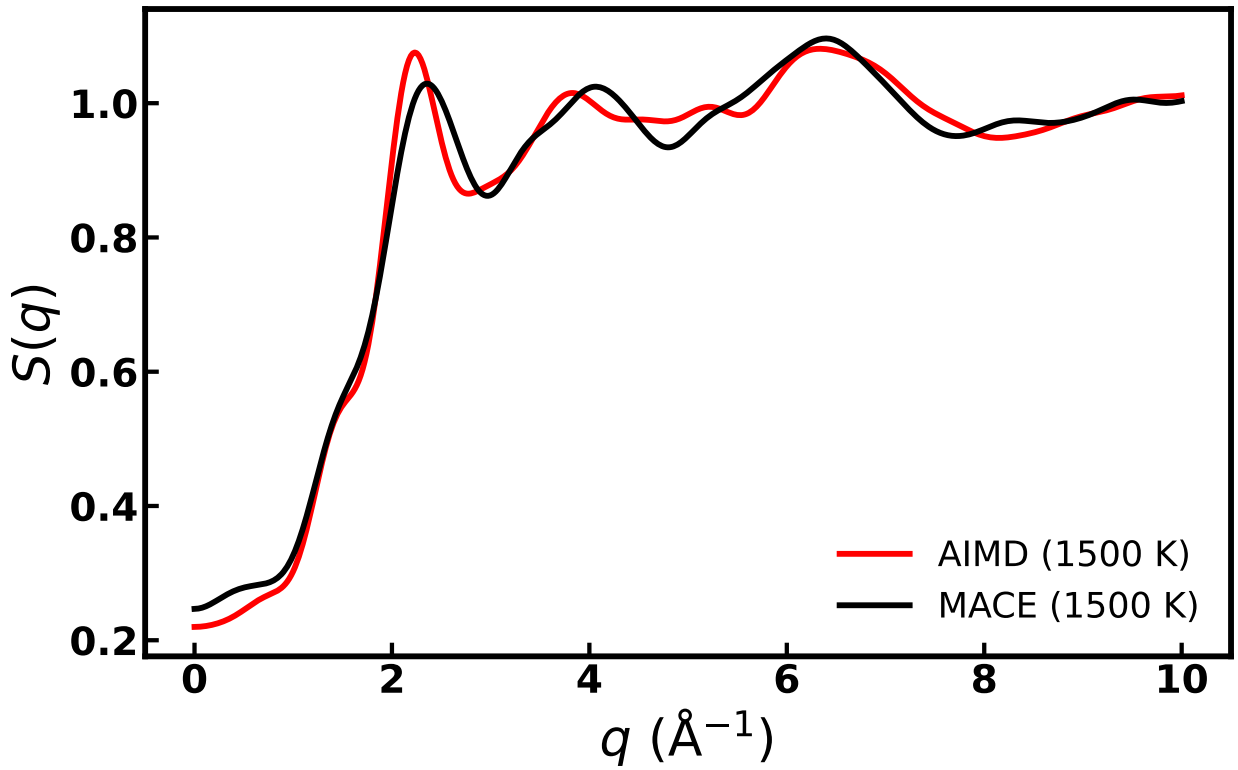

Figure 3: $S(q)$ for molten Li_2CO_3 at 1500 K, as calculated using AIMD (red) and MACE (black).

As an additional validation of the structures generated by our MACE model, we calculate the $S(q)$ at 1500 K and compare that with the AIMD data in **Figure 3**. The $S(q)$ predictions from the NequIP and MACE-MP-0 models at 1500 K are provided in **Figure S11**. The detailed methodology used to compute $S(q)$ follows previous studies [12, 74], with the necessary parameters compiled in **Table S3**. To further test the scalability and the accuracy of the MACE model, we benchmark the predictions by MACE at 1500 K in $2 \times 2 \times 2$ and $4 \times 4 \times 4$ supercells of the Li_2CO_3 structure (**Figure S13**).

Importantly, the high degree of overlap between the AIMD (red) and the MACE (black) $S(q)$ curves in **Figure 3** indicates that the MACE model successfully reproduces $S(q)$ and accurately captures the correct peak intensities as well. Additionally, we compare the MACE predictions for molten Li_2CO_3 at 1000 K with experimental $S(q)$ at 1013 K (see **Figure S12**) [13, 14] and observe remarkable similarities between the MACE predicted and experimental $S(q)$ profiles, with minor deviations occurring beyond ∼5 Å^{-1}. In the case of NequIP and MACE-MP-0, both models mostly capture the correct peak positions and peak broadening in $S(q)$ compared to AIMD, with deviations in the regions of ∼2.5 Å^{-1}, 4.5 Å^{-1} and 6 Å^{-1}, whereas MACE only shows deviations around 6 Å^{-1}.

Transport properties in Li_2CO_3

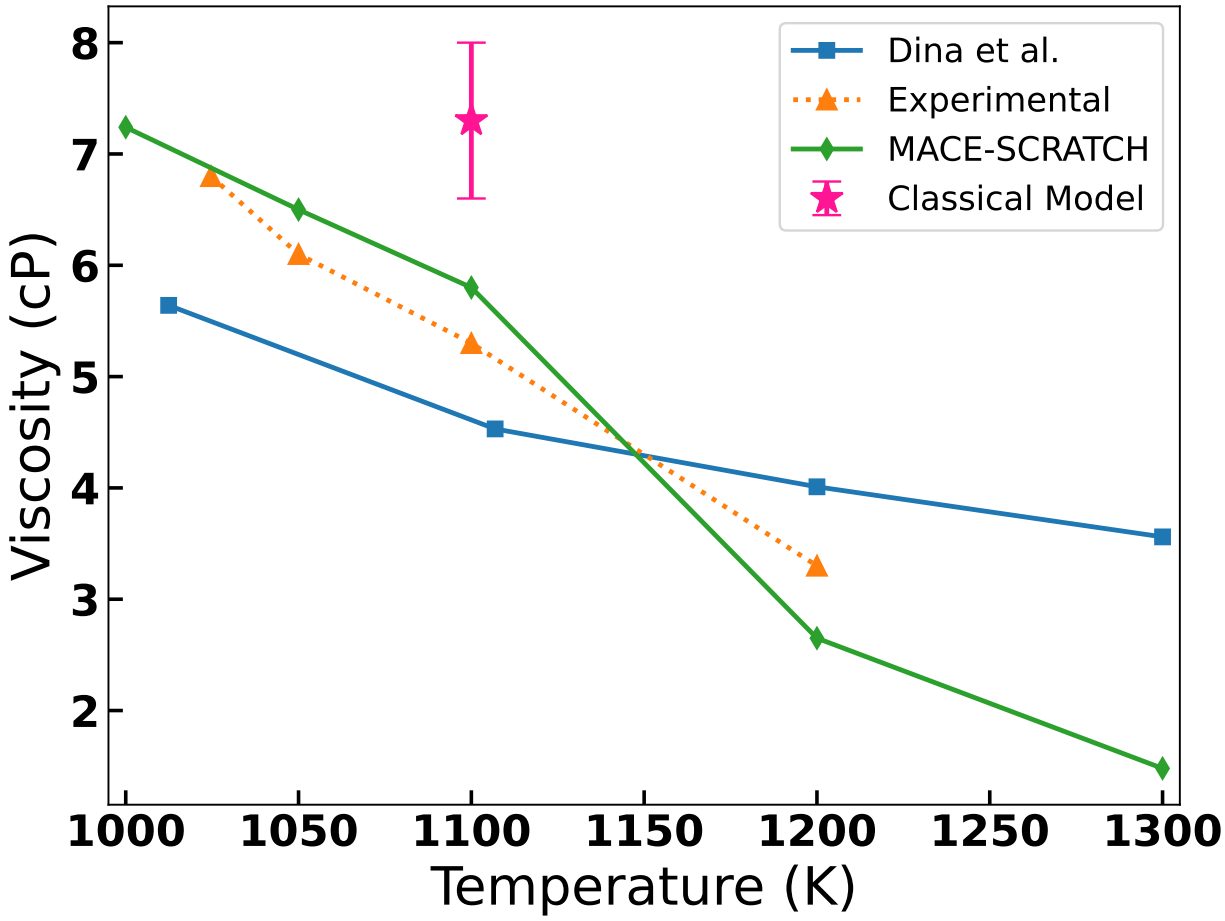

Figure 4: Viscosity of Li_2CO_3 (in units of centipoise or cP) as a function of temperature. Values predicted by the MACE-model (green) are compared with experimental data (orange), DeepMD model results (blue), and a classical force field (pink).

Given the crucial role that η plays in the flow of any molten medium, we compare the MACE-computed η at different temperatures with those from experimental [5] and computational [73, 75] studies in **Figure 4**. We also summarize the MACE-computed η in **Table S4**. Importantly, the η values predicted by our MACE model (green diamonds in **Figure 4**) closely match the experimental trends (orange triangles [5]), and significantly outperform the DeepMD model (blue squares [73]) in terms of reproducing experimental observations. Also, predictions from a classical parameterized force field [75] overestimates the experimental η at 1100 K. Thus, our optimized MACE model is able to reproduce experimental trends in η accurately compared to other computational models.

We obtain the D^* of Li^+ in Li_2CO_3 using long time-scale and large-system MD simulations, done with the MACE potential at various temperatures, and plot the results in **Figure 5**. The overall averaged MSD of individual Li^+ combining the ionic displacements along all three Cartesian directions, as a function of Δt, is presented in **Figure 5a**, with the yellow, blue, green, pink, and red curves indicating 1500 K, 1400 K, 1300 K, 1250 K, and 1000 K, respectively. **Figure 5b** plots the D^* (denoted simply as 'D' in the figure) at individual temperatures, obtained from the MSD-Δt slopes in panel a, with the color of the dots

matching the colors used in panel a. The bottom and top x-axes of **Figure 5b** correspond to $1000/T$ and T, respectively, with the slope (dashed black line) proportional to the E_a. The raw MSD-t curves containing the direction-dependent MSD of Li, at different temperatures, are compiled in **Figures S14** and **S15**.

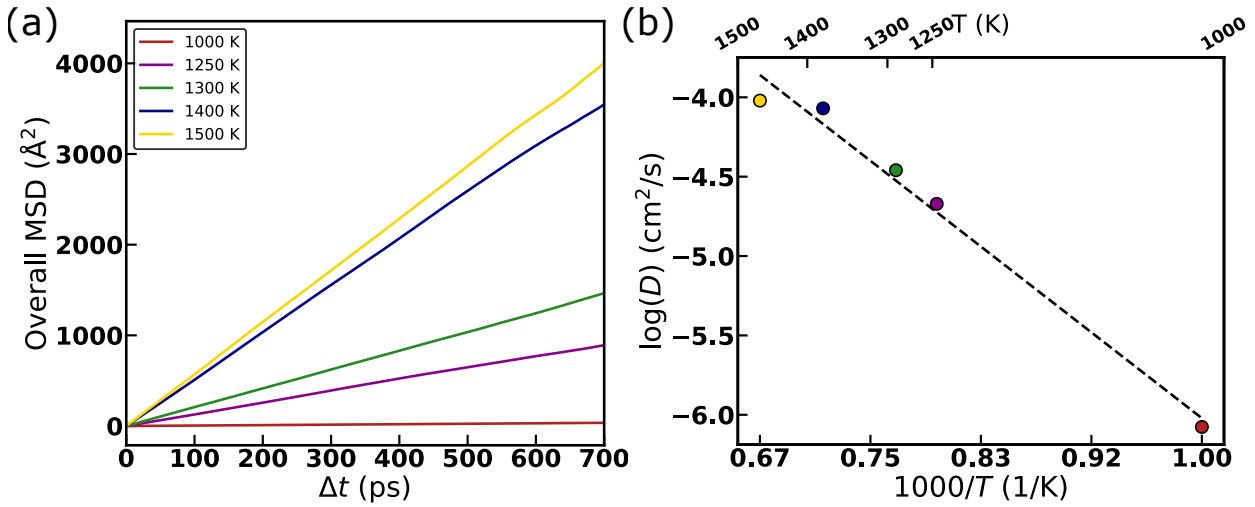

Figure 5: a) Mean-squared displacement (MSD) as a function of Δt, obtained from 700 ps MACE-MD simulations. Data are shown for five temperatures: 1500 K (yellow), 1400 K (blue), 1300 K (green), 1250 K (pink), and 1000 K (red). (b) Arrhenius representation of the diffusion coefficient, plotted as $\log D$ (with D in cm^2/s) versus $1000/T$. Symbols are color-coded according to panel (a), and the dashed black line indicates the linear fit.

At all temperatures, the MSD increases linearly with Δt, indicating diffusive behavior. Based on the MSD data, we calculate the Li^+ D^* in molten Li_2CO_3 to be 8.38×10^{-7} cm^2/s at 1000 K, 2.13×10^{-5} cm^2/s at 1250 K, 3.47×10^{-5} cm^2/s at 1300 K, 8.51×10^{-5} cm^2/s at 1400 K, and 9.53×10^{-5} cm^2/s at 1500 K, as plotted in **Figure 5b**. The Arrhenius fit of D^* with T yields an activation energy of $E_a = 1.287$ eV, with an R^2 score of 0.98. For comparison, earlier studies reported $E_a \sim 1.34$ eV [25] in molten Li_2CO_3, while diffusion studies in bulk crystalline phases reported migration barriers in the range of $0.23 - 0.49$ eV [76]. The estimated statistical uncertainty, $D^* \pm \sigma$, as obtained via block-averaging of MSD-based diffusivities is summarized in **Table S5**.

Figure S16 shows the temperature-dependent MSCD data, as a function of Δt for molten Li_2CO_3 (panel a) and the corresponding H_R (panel b), as extracted from MACE MD simulations on a $4 \times 4 \times 4$ supercell over 200 ps at 1000 K, 1300 K, and 1400 K. Importantly, H_R remains well below unity even at high temperatures, with values of 0.40 at 1400 K, 0.31 at 1300 K, and 0.20 at 1000 K, indicating that Li-ion transport in molten Li_2CO_3 is fundamentally strongly correlated. Particularly, a H_R of 0.20 (at 1000 K) indicates a significant departure from the ideal Nernst-Einstein behavior, signifying concerted migration as the dominant transport mechanism compared to uncorrelated site-to-site hopping of Li-ions. Note that the extent of correlated Li^+ motion in molten Li_2CO_3 is not immediately apparent from D^* estimates of **Figure 5a** and requires explicit calculations of MSCD and H_R. Within the ionic diffusion framework proposed by He *et al.* [77], such concerted migration events typically arise when ions in high-energy sites hop downhill, thereby causing a possible reduction in the effective energy barrier for neighboring ions that move uphill.

Additionally, we find that molten Li_2CO_3 exhibits pronounced directional anisotropy in Li^+ D^*, as revealed by the direction-dependent MSD curves at lower temperatures (**Figures S14** and **S15**). For

example, at 1000 K, the c-axis of molten Li_2CO_3 supports faster Li transport ($D_c^* > D_b^* > D_a^*$, **Figure S15**), whereas at 1400 K the three components converge to similar values (**Figure S14b**), reflecting a transition towards isotropic diffusion at elevated temperatures. Our analysis of the transient oxygen-centered Voronoi cages (i.e., regions of space closer to oxygen than other ions) in molten Li_2CO_3, through which Li^+ migrate (**Figure S17**), also supports the notion of anisotropic Li^+ motion at lower temperatures. For instance, at 1000 K (**Figure S17a**), the c-axis displays markedly smaller fluctuations in the oxygen-centered Voronoi cage volumes, compared to the a and b axes, which indicates a more persistent local topology that preferentially facilitates Li^+ transport along the c-axis. On the other hand, at 1400 K (**Figure S17b**), the cage volume fluctuations are similar along all three crystallographic directions consistent with isotropic Li^+ transport.

To further understand the concerted nature of Li^+ motion, we visualize the unwrapped trajectories of representative Li^+ motion in molten Li_2CO_3 in **Figure 6**, over 350 ps, at 1400 K (panel a) and at 1000 K (panel b). We unwrap the trajectory of motion across periodic images to improve visualization and interpretation of ionic motion. We employ a rainbow color map as a temporal marker, where blue and red denote the initial (t=0 ps) and final (t=350 ps) positions, respectively, of the ions. Importantly, the continuous nature of the Li^+ trajectories at 1400 K (**Figure 6a**) reflects the extensive migration of ions through the molten carbonate environment and signifies lower correlation among Li^+ motion. In contrast, the black circles at 1000 K (**Figure 6b**) highlight regions where Li^+ temporarily oscillate between nearby carbonate coordination sites (or cages), indicating transient trapping events before continuing its migration through the molten environment. Thus, the nature of the Li^+ concerted motion undergoes a significant change from 1000 K to 1400 K, which is also reflected in the increase in H_R from 0.2 at 1000 K to 0.40 at 1400 K (**Figure S16b**) and the increasing isotropy of Li^+ motion (**Figures S14b** and **S15**) with increasing temperatures.

The MACE-calculated RDFs further support our observations on the transient trapping of Li^+ at lower temperatures. For example, we observe pronounced Li-C peaks at ~ 3 Å and ~ 5 Å, while the Li-O exhibits a strong peak at ~ 3 Å at 1000 K (**Figure 2b**). Notably, both the Li-C and Li-O peaks appear sharper at 1000 K than at 1400 K (**Figure S5b**), indicating a more 'ordered' local coordination environment and lower thermal disorder at 1000 K compared to 1400 K. Also, the sharper Li-C and Li-O peaks at 1000 K (than at 1400 K) suggest that Li^+ experience stronger coordination with nearby carbonate groups, reflecting the possibility of (transient) trapping of Li^+ by the neighboring carbonate groups.

For elucidating the dynamic correlation among the Li-ions, we analyze the self ($G_s(r,t)$) and distinct ($G_d(r,t)$) parts of the van Hove correlation function at 1500 K, 1250 K, and 1000 K (**Figure S18**). While $G_s(r,t)$ characterizes the displacement statistics of individual ions and is directly related to the MSD, $G_d(r,t)$ probes the relative motion and spatial correlations between distinct ions. At 1500 K, we observe bright horizontal bands in $G_d(r,t)$ that rapidly decay in intensity over a 2.5 ps window, consistent with liquid-like motion. In contrast, the horizontal bands at 1250 K and 1000 K remain sharper and persist for longer timescales, particularly in the 2-6 Å range, indicating stronger transient order and more concerted motion, consistent with our previous observations in **Figures 6**, **S14-S17**. We further calculate the ionic conductivity (κ), as obtained from the Nernst- Einstein relation, plot it as a function of temperature in **Figure S19**, and compare the resultant activation energy with experimental data [5].

Discussion

In this work, we employed two equivariant graph-based MLIPs, NequIP and MACE, to understand the structure and Li-ion dynamics in molten Li_2CO_3, with broad applications in MCFCs and batteries. We

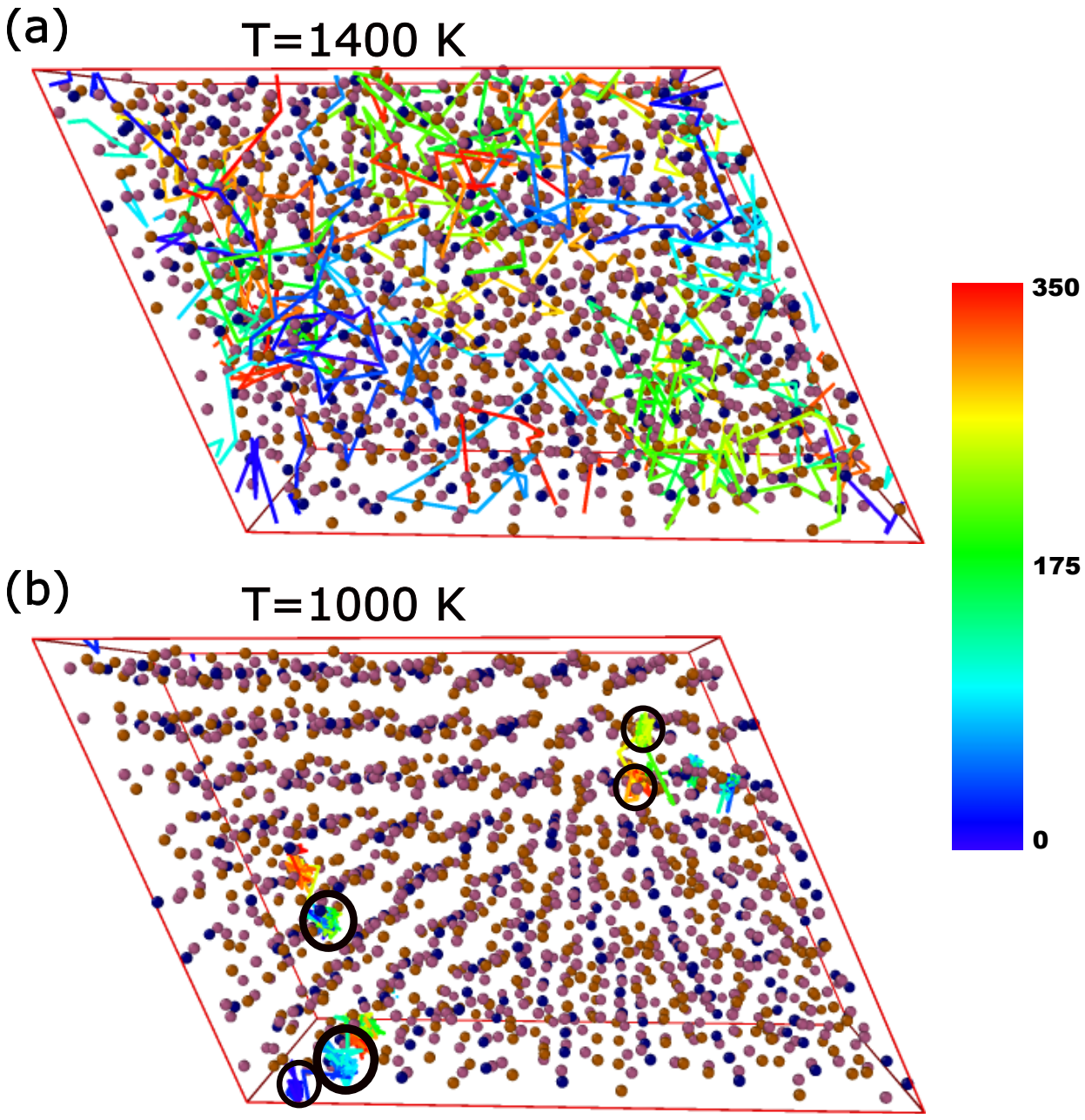

Figure 6: (a) Unwrapped diffusion trajectories of representative Li^+ in molten Li_2CO_3 at 1400 K (panel a) and at 1000 K (panel b) over 350 ps. The rainbow color map traces an ion's motion from blue (t = 0 ps) to red (t = 350 ps), depicting the temporal evolution of its path. The black circles at 1000 K mark regions of localized Li motion due to transient trapping by neighboring carbonate groups.

trained both MLIPs on *ab initio* melt-quench trajectories consisting of 3600 structures at 1500 K and 1988 structures at 1250 K (**Figure 1**). Notably, we found MACE to be the best-performing model, given its low errors on the test set (**Figures S1** and **S2**), as quantified by energy and force errors of 0.2 meV/atom and 0.17 meV/Å, respectively, on the 1000 K trajectory test set. Notably, our trained MACE model exhibited better performance than the foundational MACE-MP-0 model (without any fine-tuning) on our dataset. While fine-tuning MACE-MP-0 is a feasible strategy to accelerate MD simulations of specific systems, we

trained the MACE architecture from scratch in our work to bias the model towards maximal accuracy towards the Li_2CO_3 system.

Remarkably, our best-performing MACE model requires only two message-passing layers, while the best-performing NequIP model requires five layers (**Figure S21**), indicating the efficiency of the MACE model in learning the contributions of local bonding features to the overall potential energy surface. [47] In our benchmarking, we fixed the equivariant message-passing order to $L_{\max} = 1$ for both models to ensure a consistent comparison. However, NequIP did not achieve our optimal MACE model's accuracy even when increasing the equivariant order to $L_{\max} = 2$, indicating the superior featurization of the local geometry and the utility of including higher body-order interactions by the MACE architecture.

Given that training both models typically requires GPU acceleration, we trained the models using a single NVIDIA V100 GPU. Subsequently, the optimized MACE model was able to simulate 760 ps of molten Li_2CO_3 containing 1536 atoms within 24 hours on a NVIDIA A100 GPU. For comparison, our previous study showed that the invariant MTP model, which is not based on graph networks, was easier to train and remained more computationally efficient for MD simulations on CPUs [39, 78]. Although MACE achieved higher accuracy than NequIP in our benchmarking, it was approximately five times slower to train than NequIP with a single GPU (**Figure S21**). In CPU-based MD simulations of a 192-atom system using 16 threads on a single core, MACE was also significantly slower ($\approx 10\times$) than NequIP, highlighting the superior CPU performance of NequIP for production-scale MD (**Figure S22**). Thus, our computational speed benchmarks on both CPUs and GPUs is further indicative of the speed-accuracy trade-off that users have to optimize for in training equivariant models, which also depends on the choice of hyperparameters and the specific system itself.

We characterized the structural properties of molten Li_2CO_3 using RDFs and $S(q)$ across multiple temperatures (**Figures 2** and **3**). AIMD simulations reveal a progressive loss of medium- and long-range structural order with increasing temperature, while the strong covalent C–O bonding motif remains intact throughout the melt. The MACE model reproduces both the RDFs and $S(q)$ with high fidelity, against both AIMD and experimental data (**Figures S4**, **S11**, and **S12**) by accurately capturing the temperature dependence of peak positions and widths, and remains consistent upon scaling to larger system sizes. Furthermore, we computed the shear viscosity using MACE, which closely matches with available experimental measurements (**Figure 4**), demonstrating that the model can faithfully recover critical properties of molten Li_2CO_3.

Analysis of Li^+ transport indicated that Li-ion diffusion in molten Li_2CO_3 proceeds via highly correlated motion, as evidenced by $H_R \ll 1$ over all temperatures (**Figure S16**). While the extent of correlated motion is not immediately apparent from D^* estimates (**Figure 5**), the resultant E_a are in agreement with previous simulations [25]. Notably, direction-dependent decomposition of Li^+ MSDs (**Figures S14** and **S15**) reveal a pronounced transport anisotropy at 1000 K (with Li^+ diffusion preferred along the c-axis) and subsequent transition to a fully isotropic regime at 1400 K. Our visualization of the unwrapped Li^+ trajectories over 350 ps supports the notion of concerted motion and directional anisotropy, as indicated by transient trapping of Li^+ by carbonate cages at 1000 K (**Figure 6**). The directional anisotropy of Li^+ motion can also be linked to fewer oxygen-centered Voronoi cage fluctuations along the c-axis at 1000 K (reflecting persistent topologies that favor directional Li^+ transport) compared to 1400 K (**Figure S17**). Further, analysis of the van Hove correlation function points to a higher degree of dynamic correlation at 1000 K compared to liquid-like uncorrelated motion at 1500 K (**Figure S18**). Thus, it is clear that the extent of correlation among Li^+ motion in molten Li_2CO_3 is highly temperature dependent and tends to reduce with increasing temperatures. Although longer simulations and additional temperature sampling would improve statistical accuracy, our

calcuted MACE MD trajectories already exhibit clear temperature-dependent diffusion regimes, enabling reliable estimation of transport properties.

Conclusion

In summary, we have performed a comprehensive atomistic investigation of the structure and transport properties of molten Li_2CO_3 using equivariant MLIPs, namely MACE and NequIP. Our initial benchmarking demonstrated that the MACE model provided superior accuracy and transferability compared to NequIP and the foundational MACE-MP-0 models, based on independent test set evaluations. The structural properties predicted by our optimized MACE model, such as the persistence of the C-O pair correlation even upon melting based on RDFs and $S(q)$, show remarkable agreement with experimental and *ab initio* data. Also, our shear viscosity estimates in molten Li_2CO_3 are closer to experimental values than previous computational estimates. A central finding of our study is our prediction that Li^+ transport in molten Li_2CO_3 is fundamentally governed by highly correlated, concerted motion rather than simple, uncorrelated random hopping, as evidence by our H_R estimates that point towards a substantial deviation from the ideal Nernst-Einstein behavior. Apart from the transient trapping of Li^+ by neighboring carbonate cages contributing to the correlated motion, we also observe a high degree of directional anisotropy in Li^+ transport at lower temperatures, as characterized by the fluctuations in oxygen-centered Voronoi cage volumes and computed van Hove correlation functions. Thus, our results represent a unique temperature-dependent transition in Li^+ transport in molten Li_2CO_3, from highly correlated and anisotropic diffusion at lower temperatures to less correlated and isotropic diffusion at higher temperatures. Our work also demonstrates the utility of equivariant graph-based MLIP architectures, such as MACE, which can effectively scale to systems containing thousands of atoms and reach nanosecond timescales while maintaining near-DFT accuracy, for modelling molten systems. We hope that the insights gained in this work are useful in the optimization of MCFCs and for understanding Li^+ transport in amorphous Li_2CO_3-based SEIs.

Acknowledgments

G.S.G. acknowledges financial support from the Science and Engineering Research Board (SERB), of the Department of Science and Technology, Government of India, under sanction number IPA/2021/000007. D.D. acknowledges the Indian Institute of Science for academic support and the Shell fellowship for financial support. A.P. and A.N.K. acknowledge the support and resources provided by Shell International Exploration & Production Inc. and Shell India Markets Pvt. Ltd. A portion of the density functional theory calculations and molecular dynamics simulations showcased in this work were performed with the computational resources provided by the Supercomputer Education and Research Center, Indian Institute of Science. The authors thank Sharan Shetty, Neha Solanki, and Jason Williams at Shell for their support.

Supporting Information

Model hyperparameters, energy and force parity plots, energy fluctuations during equilibration, radial distribution functions, static structure factors, viscosity data, mean-squared-displacement and Li-ion diffusivity analysis, oxygen-centered Voronoi cage-volume analysis, van Hove correlation function calculations, ionic conductivity estimates, and computational efficiency benchmarks.

Data and code availability

All computed data and models constructed in this work are available freely for all via our GitHub repository.

Conflicts of interest

The authors have no conflicts of interest to declare.

References

[1] Masayoshi Watanabe, Morgan L Thomas, Shiguo Zhang, Kazuhide Ueno, Tomohiro Yasuda, and Kaoru Dokko. Application of ionic liquids to energy storage and conversion materials and devices. *Chemical reviews*, 117(10):7190–7239, 2017.

[2] S. McPhail, A. Moreno, and R. Bove. *International Status of Molten Carbonate Fuel Cells Technology*. ENEA, Rome, 2008.

[3] H. Ghezel-Ayagh. Advances in MCFC technology for power generation. *ECS Trans.*, 75(42):77–85, 2017.

[4] Toshikatsu Kojima, Yoshinori Miyazaki, Katsuhiro Nomura, and Kazumi Tanimoto. Density, surface tension, and electrical conductivity of ternary molten carbonate system li2co3–na2co3–k2co3 and methods for their estimation. *Journal of the Electrochemical Society*, 155(7):F150, 2008.

[5] George J Janz. Thermodynamic and transport properties for molten salts: correlation equations for critically evaluated density, surface tension, electrical conductance, and viscosity data. *Journal of physical and chemical reference data*, 17, 1988.

[6] Timothy A Barckholtz, Heather Elsen, Patricia H Kalamaras, Gabor Kiss, Jon Rosen, Dario Bove, Emilio Audasso, and Barbara Bosio. Experimental and modeling investigation of co3=/oh–equilibrium effects on molten carbonate fuel cell performance in carbon capture applications. *Frontiers in Energy Research*, 9:669761, 2021.

[7] Stephen J McPhail, Ping-Hsun Hsieh, and Jan Robert Selman. Molten carbonate fuel cells. *Materials for High-Temperature Fuel Cells*, pages 341–371, 2013.

[8] Stuart Licht, Baohui Wang, Susanta Ghosh, Hina Ayub, Dianlu Jiang, and Jason Ganley. A new solar carbon capture process: solar thermal electrochemical photo (step) carbon capture. *The Journal of Physical Chemistry Letters*, 1(15):2363–2368, 2010.

[9] Gad Licht, Kyle Hofstetter, Xirui Wang, and Stuart Licht. A new electrolyte for molten carbonate decarbonization. *Communications Chemistry*, 7(1):211, 2024.

[10] Riccardo Bini, Olga Bortolini, Cinzia Chiappe, Daniela Pieraccini, and Tiziana Siciliano. Development of cation/anion "interaction" scales for ionic liquids through esi-ms measurements. *The Journal of Physical Chemistry B*, 111(3):598–604, 2007.

[11] A Zhadan, V Sarou-Kanian, L Del Campo, L Cosson, M Malki, and C Bessada. Transport properties in molten carbonates: self-diffusion and conductivity measurements at high temperature. *International Journal of Hydrogen Energy*, 46(28):15059–15065, 2021.

[12] MC Wilding, M Wilson, OLG Alderman, CJ Benmore, JKR Weber, JB Parise, A Tamalonis, and L Skinner. Low-dimensional network formation in molten sodium carbonate sci, 2016.

[13] Francesco Sessa, Massimiliano Della Pietra, Simone Mataloni, Ana B Muñoz-García, and Michele Pavone. Structure and dynamics of li 1.24 k 0.76 co 3 molten carbonate electrolyte from molecular simulations with explicit polarization. *Physical Chemistry Chemical Physics*, 26(19):14420–14429, 2024.

[14] Hideaki Ohata, Ken Takeuchi, Koichi Ui, and Nobuyuki Koura. The structure of molten lithium carbonate calculated by dft and md simulations. *ECS Transactions*, 6(14):57, 2007.

[15] Satu Kristiina Heiskanen, Jongjung Kim, and Brett L Lucht. Generation and evolution of the solid electrolyte interphase of lithium-ion batteries. *Joule*, 3(10):2322–2333, 2019.

[16] Ben Jagger and Mauro Pasta. Solid electrolyte interphases in lithium metal batteries. *Joule*, 7(10):2228–2244, 2023.

[17] Henry Adenusi, Gregory A Chass, Stefano Passerini, Kun V Tian, and Guanhua Chen. Lithium batteries and the solid electrolyte interphase (sei)—progress and outlook. *Advanced Energy Materials*, 13(10):2203307, 2023.

[18] Luning Wang, Anjali Menakath, Fudong Han, Yi Wang, Peter Y Zavalij, Karen J Gaskell, Oleg Borodin, Dinu Iuga, Steven P Brown, Chunsheng Wang, et al. Identifying the components of the solid–electrolyte interphase in li-ion batteries. *Nature chemistry*, 11(9):789–796, 2019.

[19] Aiping Wang, Sanket Kadam, Hong Li, Siqi Shi, and Yue Qi. Review on modeling of the anode solid electrolyte interphase (sei) for lithium-ion batteries. *NPJ Computational materials*, 4(1):15, 2018.

[20] Kang Xu. Electrolytes and interphases in li-ion batteries and beyond. *Chemical reviews*, 114(23):11503–11618, 2014.

[21] Arjun S Kulathuvayal and Yanqing Su. Ionic transport through the solid electrolyte interphase in lithium-ion batteries: A review from first-principles perspectives. *ACS Applied Energy Materials*, 6(11):5628–5645, 2023.

[22] E Peled and S Menkin. Sei: past, present and future. *Journal of The Electrochemical Society*, 164(7):A1703, 2017.

[23] Takeshi Baba, Keitaro Sodeyama, Yoshiumi Kawamura, and Yoshitaka Tateyama. Li-ion transport at the interface between a graphite anode and li 2 co 3 solid electrolyte interphase: ab initio molecular dynamics study. *Physical Chemistry Chemical Physics*, 22(19):10764–10774, 2020.

[24] Xia-Xia Ma, Xin Shen, Xiang Chen, Zhong-Heng Fu, Nan Yao, Rui Zhang, and Qiang Zhang. The origin of fast lithium-ion transport in the inorganic solid electrolyte interphase on lithium metal anodes. *Small Structures*, 3(8):2200071, 2022.

[25] Laura Benitez and Jorge M Seminario. Ion diffusivity through the solid electrolyte interphase in lithium-ion batteries. *Journal of The Electrochemical Society*, 164(11):E3159, 2017.

[26] MP Tosi and FG Fumi. Ionic sizes and born repulsive parameters in the nacl-type alkali halides—ii: The generalized huggins-mayer form. *Journal of Physics and Chemistry of Solids*, 25(1):45–52, 1964.

[27] Anirban Mondal, Jeffrey M Young, Timothy A Barckholtz, Gabor Kiss, Lucas Koziol, and Athanassios Z Panagiotopoulos. Genetic algorithm driven force field parameterization for molten alkali-metal carbonate and hydroxide salts. *Journal of Chemical Theory and Computation*, 16(9):5736–5746, 2020.

[28] Reginald Mills. Self-diffusion in normal and heavy water in the range 1-45. deg. *The Journal of Physical Chemistry*, 77(5):685–688, 1973.

[29] Richard Car and Mark Parrinello. Unified approach for molecular dynamics and density-functional theory. *Physical review letters*, 55(22):2471, 1985.

[30] Dominik Marx and Jürg Hutter. *Ab initio molecular dynamics: basic theory and advanced methods*. Cambridge University Press, 2009.

[31] Jörg Behler and Michele Parrinello. Generalized neural-network representation of high-dimensional potential-energy surfaces. *Physical Review Letters*, 98(14):146401, 2007.

[32] Samuel Tovey, Anand Narayanan Krishnamoorthy, Ganesh Sivaraman, Jicheng Guo, Chris Benmore, Andreas Heuer, and Christian Holm. Dft accurate interatomic potential for molten nacl from machine learning. *The Journal of Physical Chemistry C*, 124(47):25760–25768, 2020.

[33] Albert P Bartók, Mike C Payne, Risi Kondor, and Gábor Csányi. Gaussian approximation potentials: The accuracy of quantum mechanics, without the electrons. *Physical Review Letters*, 104(13):136403, 2010.

[34] Ganesh Sivaraman, Jicheng Guo, Logan Ward, Nathaniel Hoyt, Mark Williamson, Ian Foster, Chris Benmore, and Nicholas Jackson. Automated development of molten salt machine learning potentials: application to licl. *The Journal of Physical Chemistry Letters*, 12(17):4278–4285, 2021.

[35] Alexander V Shapeev. Moment tensor potentials: A class of systematically improvable interatomic potentials. *Multiscale Modeling & Simulation*, 14(3):1153–1173, 2016.

[36] Linfeng Zhang, Jiequn Han, Han Wang, Roberto Car, and Weinan E. Deep potential molecular dynamics: a scalable model with the accuracy of quantum mechanics. *Physical review letters*, 120(14):143001, 2018.

[37] Stephen T Lam, Qing-Jie Li, Ronald Ballinger, Charles Forsberg, and Ju Li. Modeling lif and flibe molten salts with robust neural network interatomic potential. *ACS Applied Materials & Interfaces*, 13(21):24582–24592, 2021.

[38] Manh-Thuong Nguyen, Roger Rousseau, Patricia D Paviet, and Vassiliki-Alexandra Glezakou. Actinide molten salts: a machine-learning potential molecular dynamics study. *ACS Applied Materials & Interfaces*, 13(45):53398–53408, 2021.

[39] Vijay Choyal, Debsundar Dey, and Gopalakrishnan Sai Gautam. Exploration of amorphous v2o5 as cathode for magnesium batteries. *Small*, 21(45):e05851, 2025.

[40] Aqshat Seth, Rutvij Pankaj Kulkarni, and Gopalakrishnan Sai Gautam. Investigating ionic diffusivity in amorphous lipon using machine-learned interatomic potentials. *ACS Materials Au*, 5(3):458–468, 2025.

[41] Mario Geiger and Tess Smidt. e3nn: Euclidean neural networks. *arXiv preprint arXiv:2207.09453*, 2022.

[42] Simon Batzner, Albert Musaelian, and Boris Kozinsky. Advancing molecular simulation with equivariant interatomic potentials. *Nature Reviews Physics*, 5(8):437–438, 2023.

[43] Simon Batzner, Albert Musaelian, Lixin Sun, Mario Geiger, Jonathan P Mailoa, Mordechai Kornbluth, Nicola Molinari, Tess E Smidt, and Boris Kozinsky. E (3)-equivariant graph neural networks for data-efficient and accurate interatomic potentials. *Nature communications*, 13(1):2453, 2022.

[44] Ilyes Batatia, David P Kovacs, Gregor Simm, Christoph Ortner, and Gábor Csányi. Mace: Higher order equivariant message passing neural networks for fast and accurate force fields. *Advances in neural information processing systems*, 35:11423–11436, 2022.

[45] Ilyes Batatia, Simon Batzner, Dávid Péter Kovács, Albert Musaelian, Gregor NC Simm, Ralf Drautz, Christoph Ortner, Boris Kozinsky, and Gábor Csányi. The design space of e (3)-equivariant atom-centred interatomic potentials. *Nature Machine Intelligence*, 7(1):56–67, 2025.

[46] Zachary AH Goodwin, Malia B Wenny, Julia H Yang, Andrea Cepellotti, Jingxuan Ding, Kyle Bystrom, Blake R Duschatko, Anders Johansson, Lixin Sun, Simon Batzner, et al. Transferability and accuracy of ionic liquid simulations with equivariant machine learning interatomic potentials. *The Journal of Physical Chemistry Letters*, 15(30):7539–7547, 2024.

[47] Dávid Péter Kovács, Ilyes Batatia, Eszter Sara Arany, and Gabor Csanyi. Evaluation of the mace force field architecture: From medicinal chemistry to materials science. *The Journal of Chemical Physics*, 159(4), 2023.

[48] Albert Musaelian, Simon Batzner, Anders Johansson, Lixin Sun, Cameron J Owen, Mordechai Kornbluth, and Boris Kozinsky. Learning local equivariant representations for large-scale atomistic dynamics. *Nature Communications*, 14(1):579, 2023.

[49] Giacomo Tenti, Bastian Jäckl, Kousuke Nakano, Matthias Rupp, and Michele Casula. Hydrogen liquid-liquid transition from first principles and machine learning. *Physical Review B*, 112(10):104208, 2025.

[50] Harvey L Devereux, Margaret-Ann Withington, Cillian Cockrell, Kostya Trachenko, and Alin Marin Elena. Performance of the mace-mp-0 potential for calculating viscosity in lif molten salt. *arXiv preprint arXiv:2410.23679*, 2024.

[51] Anton Beiersdorfer, Lisa Hetzel, Florian Deißenbeck, Carsten Staacke, and Christopher Johannes Stein. Gap vs. mace: Efficiency evaluation in a liquid electrolyte system. *Machine Learning: Science and Technology*, 2025.

[52] Ilyes Batatia, Philipp Benner, Yuan Chiang, Alin M Elena, Dávid P Kovács, Janosh Riebesell, Xavier R Advincula, Mark Asta, Matthew Avaylon, William J Baldwin, et al. A foundation model for atomistic materials chemistry. *The Journal of chemical physics*, 163(18), 2025.

[53] Ganesh Kumar Nayak, Prashanth Srinivasan, Juraj Todt, Rostislav Daniel, Paolo Nicolini, and David Holec. Accurate prediction of structural and mechanical properties on amorphous materials enabled through machine-learning potentials: A case study of silicon nitride. *Computational Materials Science*, 249:113629, 2025.

[54] Wanderlã L Scopel, Antônio JR da Silva, and Adalberto Fazzio. Amorphous hfo 2 and hf 1- x si x o via a melt-and-quench scheme using ab initio molecular dynamics. *Physical Review B—Condensed Matter and Materials Physics*, 77(17):172101, 2008.

[55] Mariette Hellenbrandt. The inorganic crystal structure database (icsd)—present and future. *Crystallography Reviews*, 10(1):17–22, 2004.

[56] Quanying Yan, Chenyu Wang, Chao Liu, and Jing Zhang. Experimental and theoretical research on the thermal properties of carbonate mixtures. In *IOP Conference Series: Materials Science and Engineering*, volume 729, page 012031. IOP Publishing, 2020.

[57] Georg Kresse and Jürgen Furthmüller. Efficiency of ab-initio total energy calculations for metals and semiconductors using a plane-wave basis set. *Computational materials science*, 6(1):15–50, 1996.

[58] Georg Kresse and Jürgen Furthmüller. Efficient iterative schemes for ab initio total-energy calculations using a plane-wave basis set. *Physical review B*, 54(16):11169, 1996.

[59] Georg Kresse and Daniel Joubert. From ultrasoft pseudopotentials to the projector augmented-wave method. *Physical review b*, 59(3):1758, 1999.

[60] John P Perdew, Kieron Burke, and Matthias Ernzerhof. Generalized gradient approximation made simple. *Physical review letters*, 77(18):3865, 1996.

[61] Hendrik J Monkhorst and James D Pack. Special points for brillouin-zone integrations. *Physical review B*, 13(12):5188, 1976.

[62] Aidan P Thompson, H Metin Aktulga, Richard Berger, Dan S Bolintineanu, W Michael Brown, Paul S Crozier, Pieter J In't Veld, Axel Kohlmeyer, Stan G Moore, Trung Dac Nguyen, et al. Lammps-a flexible simulation tool for particle-based materials modeling at the atomic, meso, and continuum scales. *Computer physics communications*, 271:108171, 2022.

[63] William G Hoover. Canonical dynamics: Equilibrium phase-space distributions. *Physical review A*, 31(3):1695, 1985.

[64] Loup Verlet. Computer" experiments" on classical fluids. i. thermodynamical properties of lennard-jones molecules. *Physical review*, 159(1):98, 1967.

[65] Aris Marcolongo and Nicola Marzari. Ionic correlations and failure of nernst-einstein relation in solid-state electrolytes. *Physical Review Materials*, 1(2):025402, 2017.

[66] Adolph Fick. V. on liquid diffusion. *The London, Edinburgh, and Dublin Philosophical Magazine and Journal of Science*, 10(63):30–39, 1855.

[67] Xingfeng He, Yizhou Zhu, Alexander Epstein, and Yifei Mo. Statistical variances of diffusional properties from ab initio molecular dynamics simulations. *npj Computational Materials*, 4(1):18, 2018.

[68] Gopalakrishnan Sai Gautam and Pieremanuele Canepa. Theoretical modelling of multivalent ions in inorganic hosts. 2019.

[69] Yifei Mo, Shyue Ping Ong, and Gerbrand Ceder. First principles study of the li10gep2s12 lithium super ionic conductor material. *Chemistry of Materials*, 24(1):15–17, 2012.

[70] Shyue Ping Ong, Yifei Mo, William Davidson Richards, Lincoln Miara, Hyo Sug Lee, and Gerbrand Ceder. Phase stability, electrochemical stability and ionic conductivity of the li 10±1 mp 2 x 12 (m= ge, si, sn, al or p, and x= o, s or se) family of superionic conductors. *Energy & Environmental Science*, 6(1):148–156, 2013.

[71] S Plumari, A Puglisi, F Scardina, and V Greco. Shear viscosity of a strongly interacting system: Green-kubo correlator versus chapman-enskog and relaxation-time approximations. *Physical Review C—Nuclear Physics*, 86(5):054902, 2012.

[72] Elsa Desmaele, Nicolas Sator, Rodolphe Vuilleumier, and Bertrand Guillot. Atomistic simulations of molten carbonates: thermodynamic and transport properties of the li2co3—na2co3—k2co3 system. *The Journal of Chemical Physics*, 150(9), 2019.

[73] Dina Kussainova and Athanassios Z Panagiotopoulos. Molecular simulation of lithium carbonate reactive vapor–liquid equilibria using a deep potential model. *Journal of Chemical & Engineering Data*, 69(1):204–214, 2023.

[74] Samuel Tovey, Anand Narayanan Krishnamoorthy, Ganesh Sivaraman, Jicheng Guo, Chris Benmore, Andreas Heuer, and Christian Holm. Dft accurate interatomic potential for molten nacl from machine learning. *The Journal of Physical Chemistry C*, 124(47):25760–25768, 2020.

[75] Anirban Mondal, Jeffrey M Young, Timothy A Barckholtz, Gabor Kiss, Lucas Koziol, and Athanassios Z Panagiotopoulos. Genetic algorithm driven force field parameterization for molten alkali-metal carbonate and hydroxide salts. *Journal of Chemical Theory and Computation*, 16(9):5736–5746, 2020.

[76] Hakim Iddir and Larry A Curtiss. Li ion diffusion mechanisms in bulk monoclinic li2co3 crystals from density functional studies. *The Journal of Physical Chemistry C*, 114(48):20903–20906, 2010.

[77] Xingfeng He, Yizhou Zhu, and Yifei Mo. Origin of fast ion diffusion in super-ionic conductors. *Nature communications*, 8(1):15893, 2017.

[78] Vijay Choyal, Nidhish Sagar, and Gopalakrishnan Sai Gautam. Constructing and evaluating machine-learned interatomic potentials for li-based disordered rocksalts. *Journal of chemical theory and computation*, 20(11):4844–4856, 2024.